

## Article

# Metatungstate Chemical Vapor Deposition of WSe<sub>2</sub>: Substrate Effects, Shapes, and Morphologies

Krastyo Buchkov <sup>1,\*</sup>, Peter Rafailov <sup>1</sup>, Nikolay Minev <sup>2</sup>, Vladimira Videva <sup>2,3</sup>, Velichka Strijkova <sup>2</sup>, Todor Lukanov <sup>2</sup>, Dimitre Dimitrov <sup>1,2</sup> and Vera Marinova <sup>2</sup>

<sup>1</sup> Institute of Solid State Physics, Bulgarian Academy of Sciences 72, Tzarigradsko Chaussee Blvd, 1784 Sofia, Bulgaria; rafailov@issp.bas.bg (P.R.); dzdimitrov@issp.bas.bg (D.D.)

<sup>2</sup> Institute of Optical Materials and Technologies, Bulgarian Academy of Sciences, Acad. G. Bontchev Str. 109, 1113 Sofia, Bulgaria; nminev@iomt.bas.bg (N.M.); vvideva@iomt.bas.bg (V.V.); vily@iomt.bas.bg (V.S.); tlukanov@iomt.bas.bg (T.L.); vmarinova@iomt.bas.bg (V.M.)

<sup>3</sup> Faculty of Chemistry and Pharmacy, Sofia University, 1 James Bourchier Blvd., 1164 Sofia, Bulgaria

\* Correspondence: buchkov@issp.bas.bg

**Abstract:** Owing to their exceptional properties, which are usually determined by the growth conditions, 2D transition metal dichalcogenides (TMDCs) offer numerous research directions for applications in the fields of spintronics, valleytronics, and optoelectronics. Here, we focus on the chemical vapor deposition (CVD) synthesis of WSe<sub>2</sub> (tungsten diselenide) nanoclusters/nanoflakes by using a liquid precursor for tungsten (ammonium metatungstate) on Si/SiO<sub>2</sub>, fused silica, and sapphire substrates. Various WSe<sub>2</sub> clusters with different sizes, thicknesses, and geometries were analyzed by means of optical and atomic force microscopy (AFM) and Raman spectroscopy. The observed structures were mostly WSe<sub>2</sub> multilayers; however, monolayer formations were also found. They showed significant morphological differences, as well as wide nucleation density and size variations, possibly related to precursor/substrate surface interactions under the same CVD synthesis conditions. The largest WSe<sub>2</sub> domains with a lateral size of up to hundreds of micrometers were observed on sapphire, probably caused by a higher growth rate of singular nucleation sites. WSe<sub>2</sub> domains with irregular and triangular shapes were simultaneously identified on fused silica, whereas multilayered pyramidal WSe<sub>2</sub> structures dominated in the case of Si/SiO<sub>2</sub> substrates. The application of polarized Raman spectroscopy to precisely determine and differentiate the characteristic vibrational modes (A<sub>1g</sub>, E<sub>2g</sub>, and 2LA(M)) enabled the unambiguous identification of 2D and/or multilayered WSe<sub>2</sub> formations with a high crystallinity level. The presented comparative analysis of samples prepared in relatively simple synthesis conditions (moderate working temperatures and ambient pressure) provides a base for further progress of the facile metatungstate CVD method and relevant opportunities for the exploration of 2D TMDC materials.

**Keywords:** tungsten diselenide; chemical vapor deposition; Raman spectroscopy; atomic force microscopy



**Citation:** Buchkov, K.; Rafailov, P.; Minev, N.; Videva, V.; Strijkova, V.; Lukanov, T.; Dimitrov, D.; Marinova, V. Metatungstate Chemical Vapor Deposition of WSe<sub>2</sub>: Substrate Effects, Shapes, and Morphologies. *Crystals* **2024**, *14*, 184. <https://doi.org/10.3390/cryst14020184>

Academic Editors: Yijing Y. Stehle, Fangzhu Qing, Dmitri Donetski and Francisco M. Morales

Received: 9 December 2023

Revised: 5 January 2024

Accepted: 9 January 2024

Published: 13 February 2024



**Copyright:** © 2024 by the authors. Licensee MDPI, Basel, Switzerland. This article is an open access article distributed under the terms and conditions of the Creative Commons Attribution (CC BY) license (<https://creativecommons.org/licenses/by/4.0/>).

## 1. Introduction

The unique 2D physical nature of transition metal dichalcogenide (TMDC) materials offers numerous research directions in the fields of spintronics, valleytronics, and optoelectronics due to the materials' exceptional properties, which are predominantly determined by the growth conditions.

The TMDC materials' individual electronic band structure creates a unique spectrum of topological, magnetic, and electric phenomena. Tungsten diselenide [1–4] is a widely studied material that belongs to the constantly progressing group of layered 2D materials [5]. As is typical for 2D TMDCs, the manifestation of various physical properties in WSe<sub>2</sub> depends on the layer number due to the weak van der Waals interlayer and strong intralayer ionic/covalent bonding.

The distinctive physical characteristics of WSe<sub>2</sub> include p-type semiconductor behaviors with strong spin–orbital coupling [6], a low thermal conductivity [7], a direct/indirect band gap [8] evolving with the number of layers [9], and corresponding intense excitonic [10] and light–matter interaction effects [11]. The combination of these properties offers perspectives for a variety of WSe<sub>2</sub>-based spintronic [12], valleytronic [13], and optoelectronic devices. In addition, the broad set of TMDC properties is highly dependent on the structural configurations and the thickness/number of layers, which are determined by the synthesis approach. Currently, the fundamental and practical WSe<sub>2</sub> investigations [2–4] are dependent on the development of techniques such as chemical vapor deposition (CVD) [14–16] and preparation strategies such as mechanical exfoliation and transfer [17–21].

The CVD synthesis of W-based TMDC [20] is challenging due to the high melting (evaporation/sublimation) points, requirements for low vapor pressures, minimal electronegativity ratio with chalcogenide elements, and limited chemical reactivity (especially for Te). In order to achieve suitable growth conditions, an efficient CVD process requires the use of high-volatility precursors, an enriched H<sub>2</sub> carrier/reactive gas atmosphere (and/or low pressure), and heterogenic approaches using additional reagents as reaction catalysts, growth and eutectics promoters [22–25]. However, until technological feasibility and scalability requirements are met, there are many remaining obstacles to precise control over all the variables of nucleation, growth, and coalescence processes toward the realization of continuous 2D films.

Generally, powdered WO<sub>3</sub> is the most widely used precursor, along with various W-based carbonates, hexachlorides, and oxychlorides [26,27] (for metal–organic CVD). To accomplish synthesis in a 2D form, the conventional CVD method uses the vapor–solid–solid (VSS) mechanism based on WO<sub>3</sub> adsorption on the substrate and corresponding chemical reactions facilitated through surface chalcogenide diffusion [28–32].

Other prospective precursor groups include sodium tungstate Na<sub>2</sub>WO<sub>4</sub> [33] and complex ammonia compounds such as metatungstate hydrate (AMT) (NH<sub>4</sub>)<sub>6</sub>[H<sub>2</sub>W<sub>12</sub>O<sub>40</sub>]·nH<sub>2</sub>O [34–40]. These precursors have been used for a vapor–liquid–solid (VLS) CVD process [25], as well as low-temperature hydro(solvo)thermal and template-assisted synthesis [21] for the preparation of Mo- [41,42] and V-based TMDC systems [37–39].

As an alternative, metatungstate precursors are widely accessible from chemistry suppliers and are less toxic compared with the conventional W-based chloride and oxycarbonate reagents. Furthermore, we must note their suitable aqueous solubility (in contrast to WO<sub>3</sub>), which provides unique options for solution-based direct deposition over various substrates and the practical advantage of a single-step conformal TMDC coating over 3D structures such as optical fibers [43], which is not accessible in VSS CVD. This can effectively simplify the CVD process requirements regarding the thermal and hydrogen-enriched reaction atmosphere conditions.

Moreover, this approach allows for particular control of the location and size of the growing TMDC seed islands [41] for the formation of 1D structures (nanowires) [18], 2D clusters (flakes and ribbons) [44], and 3D forms (pyramids) [45]. Another advantageous aspect is the possibility of chemical modifications via precursor mixing [36–40,46] and more precise doping for tailoring of the electronic, optical, and magnetic properties. The unique prospects of the liquid phase precursor method [47] have also been developed toward the preparation of lateral TMDC hetero-interfaces as well as the implementation of industrial inkjet printing [48] and robust patterned deposition control [49] of 2D MoSe<sub>2</sub>, MoS<sub>2</sub>, WSe<sub>2</sub>, and SnSe<sub>2</sub> layers [50].

One of the main synthesis challenges in liquid precursor-mediated CVD is related to the chemical complexity of the starting reagents. Principally, this could lead to a higher level of structural disorder in the final TMDC structures and limited practical performance of base electronic devices, such as the field-effect transistor (FET). Nevertheless, there are reports of prototype TMDC FET devices produced via the VLS approach that show

characteristics (electron mobility, on–off ratio, and threshold voltage range) [51] comparable with those of devices fabricated using the conventional VSS precursors.

The metatungstate precursor can be utilized together with the large family of alkali metal growth promoters [52–54], which include organic sodium cholate (SC) hydrate ( $C_{24}H_{39}NaO_5 \cdot nH_2O$ ), sodium hydroxide, and conventional salts [22,55,56]. These reagents have a positive effect on the CVD process by increasing the surface substrate/precursor adhesive adatom energy, thereby improving the eutectic and catalytic conditions for the chemical reactions by forming the necessary intermediate complexes [25,57].

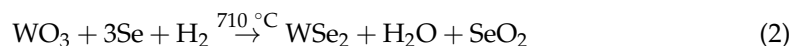
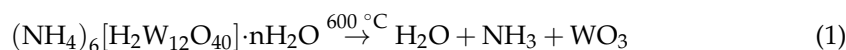
To the best of our knowledge, the synthesis of  $WSe_2$  (or  $WS_2$ ,  $WTe_2$ ) using the metatungstate/sodium cholate method is mainly applied on Si/SiO<sub>2</sub> substrates (and, very recently, on soda lime glass [48]) and is rather unexplored in the case of sapphire (using  $Na_2WO_4$  [58]) and fused silica substrates. The high synthesis temperatures required for the vapor–solid CVD growth of  $WSe_2$  on quartz and sapphire [28–32] result in significant strain effects and an unusual step-edge-guided layer-over-layer growth process (in the latter case).

In the present study, we are focusing on the CVD synthesis of  $WSe_2$  using AMT as the main precursor, together with SC as a heterogeneous nucleation and growth promoter. Because TMDC's growth process is determined by the dynamic eutectic interactions of the precursor/substrate interface, the experiments were performed using Si/SiO<sub>2</sub>, fused silica, and c-cut sapphire. In addition, an auxiliary study measuring the wettability (contact angle) and hydrophilic properties of the tungstate/cholate aqueous solution is presented. Following a CVD process with several facile steps (the specific details of which are presented herein), peculiar  $WSe_2$  cluster formations of different geometry, size, and thickness were obtained and analyzed by means of optical microscopy, AFM, and Raman spectroscopy. The observed sophisticated growth morphology related to the synthesis conditions and substrate/interface effects provides a base for further improvements and opens up novel directions in TMDC synthesis.

## 2. Materials and Methods

### 2.1. Precursor Deposition and CVD Synthesis Procedure

The base chemical reaction of  $WSe_2$  formation relies on the relatively low (600 °C) decomposition temperature (1) [59] of metatungstate  $(NH_4)_6[H_2W_{12}O_{40}] \cdot nH_2O$  ( $n = 1–22$ , CAS No. 12333-11-8) to stable m-WO<sub>3</sub> (monoclinic), which then reacts with the Se vapor phase through the Ar/H<sub>2</sub> carrier gas (2) and intermediate gaseous precursor H<sub>2</sub>Se. The H<sub>2</sub> gas also acts as a reducing reaction agent for  $WSe_2$  formation via the VLS method [33].



Sodium cholate is an anionic, amphiphathic complex consisting of both hydrophilic and hydrophobic radicals; thus, it is utilized as a stabilizing surfactant (such as in liquid phase exfoliation [60]) with the important role of enhancing the precursor's adsorption on the substrate [61] and facilitating TMDC growth. Reaction (2) is also possibly mediated by SC, leading to the formation of intermediate Na-based byproduct compounds [62]. The exact nature of the entire set of chemical, crystallization, and growth processes of the liquid precursor-intermediated CVD approach is not yet fully understood [44,63]. We presume that it is similar to the model proposed recently for  $Na_2WO_4$  [33] (Mo [64,65], Nb [66]) complexes within the framework of the vapor–liquid–solid mechanism for TMDC, where the eutectic precursor phase/substrate interface [66] and thermodynamic nucleation evolution [67,68] play key roles.

To prepare the aqueous solution precursor, we used 0.025 g of metatungstate (Alfa Aesar, CAS No. 12333-11-8) and 0.1 g of sodium cholate (Alfa Aesar CAS No. 206986-87-0) in 5 mL of deionized water, giving a mass ratio of 0.4:1:50, which is close to the principal (3.1 mM) solubility limit of the metatungstate [39]. We observed that after

one week, the solution formed coagulated particles (probable SC micelle aggregation), which is detrimental for the next stages of the synthesis process; therefore, the aqueous precursor mixture was prepared shortly before the synthesis. In addition, the wettability and corresponding contact angles of the precursor solution were preliminary determined using a drop shape analyzer (via the sessile drop technique). The measured contact angle values are presented in Figure 1a and were as follows:  $15^\circ$  for Si/SiO<sub>2</sub>,  $39^\circ$  for fused silica, and  $32^\circ$  for sapphire. These values indicate suitable wettability due to the salinity of the solution. This indirectly suggests a moderate surface energy as a key parameter determining the level of precursor molecule adhesion over the substrates. The spin coating uniformity is also limited by the low solubility of the tungstate/cholate mixture. Correspondingly, we performed several experiments to determine the optimal parameters for homogenous deposition over the substrate, achieved by means of dynamic spin coating (for 60 sec) in the range of 6000–8000 rpm. The precursor solution was applied in microliter droplet amounts (after the initial spinning acceleration), considering the type of the selected substrate (Si/SiO<sub>2</sub>, sapphire, and fused silica), to a final amount of approximately  $10 \div 25 \mu\text{L}/\text{cm}^2$  (shown in Figure 1b for Si/SiO<sub>2</sub>).

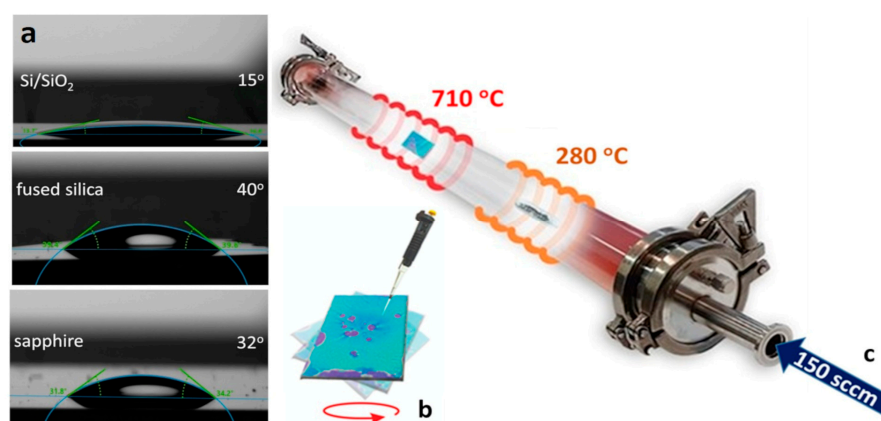


**Figure 1.** (a) Contact angles of the metatungstate/cholate aqueous solution over the substrates; (b) spin-coated precursor over Si/SiO<sub>2</sub>; (c) schematic and parameters of the CVD process.

The main parameters and a schematic of the CVD synthesis process in a three-zone quartz tube reactor are presented in Figure 1c. The substrates covered with tungstate/cholate were placed in the central furnace zone ( $\sim 710^\circ\text{C}$ ), and the direct chemical selenization reaction was maintained by using ultra-high-purity Se (5 N/1  $\div$  1.5 g) shots in a quartz boat in the upstream thermal zone ( $\sim 280^\circ\text{C}$ ). The heating rates for the Se zone ( $18^\circ\text{C}/\text{min}$ ) and WSe<sub>2</sub> growth zone ( $44^\circ\text{C}/\text{min}$ ) were synchronized to reach the target temperatures simultaneously. This was followed by a 2 h dwell stage at  $710^\circ\text{C}$  for the selenization and growth (nucleation) process. The third (empty) zone was set to  $730^\circ\text{C}$  to improve the thermal plateau in the reaction zone. The CVD process was mediated under a 150 sccm flow of an Ar (90%)/H<sub>2</sub> (10%) reactive carrier gas mixture. The pre-synthesis reactor atmosphere purge procedure was performed with the same gas mixture for 45 min.

## 2.2. Experimental Techniques

The growth features, shape formations, and layer thickness of deposited WSe<sub>2</sub> were analyzed by means of optical and atomic force microscopy and polarized Raman spectroscopy.

The following standard substrates were used: Si/SiO<sub>2</sub> (with a 300 nm oxide layer), fused silica (JGS2, with both sides polished and an rms roughness of  $<1$  nm), and c-cut sapphire (synthetic standard with an rms roughness of  $\sim 0.3$  nm) supplied by Ossila. Before the spin coating deposition of the precursor solution, the substrates were cleaned by standard wet chemistry protocols. No additional pre-treatments to modify the substrate surface were applied. The substrates' wettability regarding the aqueous (DI) tungstate/cholate

solution was determined by measuring the contact angle using a Krüss DSA25S drop shape analyzer.

Optical microscopy images of WSe<sub>2</sub> clusters were observed using an Olympus BX53 microscope with reflected and scattered light in the dark field (DF) mode.

The Raman spectrum characterization was performed using a HORIBA Jobin Yvon Labram HR visible spectrometer in a backscattering geometry with a He-Ne laser (excitation wavelength at 633 nm). A high-resolution 1800 lines mm<sup>-1</sup> grating was used, which was needed particularly to distinguish the close-lying WSe<sub>2</sub> Raman peaks. Si standard and neon lines were used to calibrate the frequency, and the Raman line parameters were determined by means of fitting to Voigt profiles. The scattered radiation was captured using a CCD detector. The laser power was kept below 0.5 mW to avoid heating damage to the layers and corresponding measurement artifacts.

The nanoscale surface topography and thickness profile were analyzed using an Asylum Research MFP-3D atomic force microscope in the standard AC tapping mode (AC160TS-R3 tips).

### 3. Characterization and Analysis

#### 3.1. Metastable Method for WSe<sub>2</sub> Deposition on Si/SiO<sub>2</sub>

TMDC cluster synthesis is related to the crystal lattice symmetry of the given compound (hexagonal 2H for WSe<sub>2</sub> or, for instance, orthorhombic 1T for WTe<sub>2</sub>) and can occur in typical triangle, hexagon [69], or nanobelt flake patterns [70]. The lateral size and shape of the clusters depend on the chemical potentials of the reacting elements and a favorable edge growth energy [71], which is determined by the CVD synthesis parameters, precursor types, and substrate effect.

In the case of WSe<sub>2</sub> cluster formation on Si/SiO<sub>2</sub> substrate via the metastable approach, the optical microscopy observations show the expected equilateral triangular structures (Figure 2a,b), with sizes ranging between 3 and 10 μm.

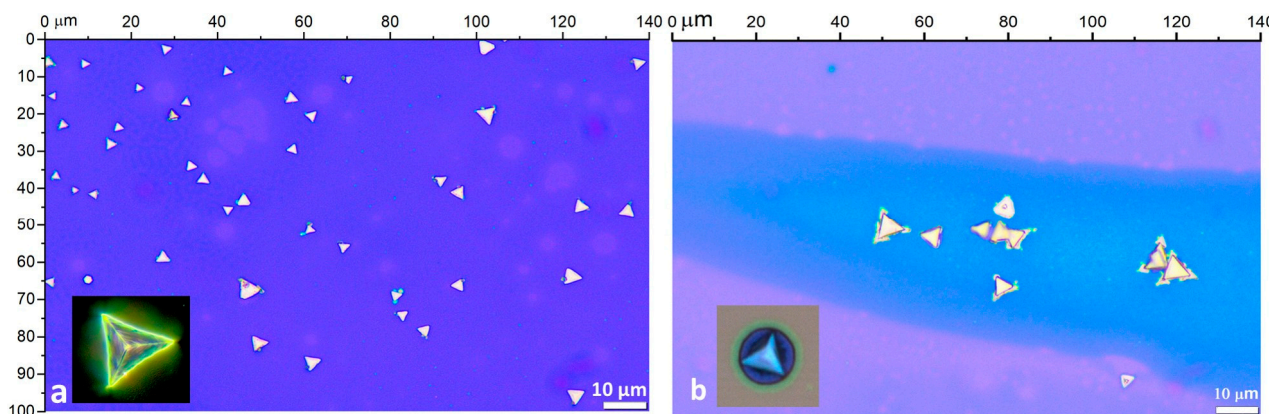


**Figure 2.** Optical images of WSe<sub>2</sub> on Si/SiO<sub>2</sub> under reflected illumination: 100× magnification of equilateral flakes (a,b) with an enlarged view in DF mode ((a), inset) and local substrate corrosive effects ((b), inset) around the WSe<sub>2</sub> pyramids.

However, the coverage and distribution density over the substrate area are relatively low, and clusters mostly formed in scattered groups within the zones with higher precursor accumulation during the spin coating deposition process. The kinks formations at the vertices and edges of some of the triangular domains (Figure 2b) are typical morphological features of VLS growth. These are usually developed as a crystallization irregularity due to a non-uniform molten precursor concentration at the liquid–solid interface [66,72]. In addition, the VLS process of binding the precursor’s nucleus onto the silicon oxide layer can cause local corrosive effects [54] (in the formed cluster’s vicinity), as shown in the inset image of Figure 2b.

The observed faceted morphology of the majority of the clusters (in the enlarged DF image), together with the AFM height profiles and the Raman data (presented in Figure 3a,b), reveals a predominantly vertical growth of thick multilayered WSe<sub>2</sub> in a pyramidal form. The WSe<sub>2</sub> pyramid apex thickness can reach up to hundreds of nanometers depending on the particular cluster size. Both the edge/side wall cross-sections are presented as profile graphs in Figure 3b.

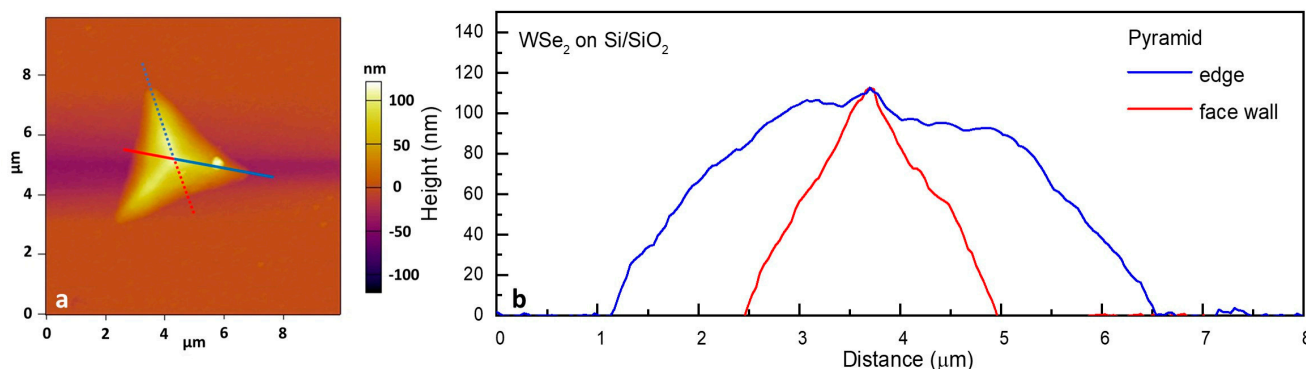


**Figure 3.** AFM analysis of WSe<sub>2</sub> on Si/SiO<sub>2</sub> with a thickness map (a) and profiles of the pyramidal clusters (b).

As noted in the Introduction, the various TMDC growth structures often demonstrate unique physical properties [73–75]. For instance, pyramidal MoS<sub>2</sub> structures [76] show sophisticated helical electrical current flow [77] and, additionally, high energy harvesting capabilities through an electrocatalytic hydrogen evolution reaction [78]. Among the TMDC clusters with similar 3D geometry, altered optical, magnetic, catalytic, and electrical properties were also found for MoS<sub>2</sub> (strong excitonic absorption and cathodoluminescence [79]), WS<sub>2</sub> (complex Raman spectrum [80], non-linear optical response, and catalytic activity [81,82]), WSe<sub>2</sub> [83,84] (plasmonic effects), and in anti-pyramidal MoS<sub>2</sub>/WS<sub>2</sub> vertical heterostructures [58] prepared via a VLS growth process.

A record non-linear optical (second and third harmonic) response and strong light-matter interactions were observed for nanopyramidal MoTe<sub>2</sub> [45] (obtained via liquid precursor-mediated CVD) with an edge-rich structure. In addition, higher optical harmonics generation was investigated for WS<sub>2</sub> with enhanced intensity as the thickness increased [82], reaching several orders of magnitude for a thickness (~100 nm) comparable with that in our case.

The Raman signal sensitivity regarding peak positions, shifts, and intensity relations provides quite reliable indications of the TMDC thickness (and, consequently, the layer number) [85–88]. Typically, for WSe<sub>2</sub>, the main Raman modes are the A<sub>1g</sub> mode, caused by out-of-phase vibrations of the Se sublattice perpendicular to the layer planes, and the weaker E<sub>2g</sub> peak, attributed to in-plane oscillations of both tungsten and selenium atoms; however, their spectral positions are very close to each other, at around 250 cm<sup>-1</sup>.

These first-order phonons appear within a broad band consisting of second-order features, dominated by the exceptionally intense 2LA(M) mode, appearing typically at 633 nm excitation due to excitonic resonance. For single-layer WSe<sub>2</sub>, the E<sub>2g</sub> mode is expected to be virtually degenerate with A<sub>1g</sub>—both lying between 249.5 and 250 cm<sup>-1</sup> [88]. With an increasing layer number, A<sub>1g</sub> slightly hardens while E<sub>2g</sub> softens, and the frequency distance between these modes saturates at about 3 cm<sup>-1</sup> for thicknesses approaching those of bulk samples [88]. As can be expected from the different vibrational patterns of both modes, the Raman intensity ratio I(A<sub>1g</sub>)/I(E<sub>2g</sub>) sharply increases with the layer number. The 2LA(M) band undergoes a downshift from ~261 cm<sup>-1</sup> to ~257 cm<sup>-1</sup> with increasing WSe<sub>2</sub> thickness from monolayers to trilayers [85–88]. Taken together, these dependencies can enable a semiquantitative estimate of the WSe<sub>2</sub> thickness. The possible presence of a faint peak close to 308 cm<sup>-1</sup> could be considered as an additional indication. This peak,

which is assigned to the forbidden  $B_{2g}^1$  mode (modulating the vertical W-Se bond) by some authors, is reportedly activated in the Raman spectrum of multilayered  $WSe_2$  by van der Waals interactions between adjacent layers [88]. In order to accurately identify the corresponding spectral tendencies for the  $WSe_2$  layers, polarized backscattering Raman spectroscopy was implemented using the opposite polarization properties of the  $A_{1g}$  and  $E_{2g}$  modes, with  $A_{1g}$  being allowed only in parallel ( $Z(Y\bar{Y})\bar{Z}$ ) and  $E_{2g}$  only in crossed ( $Z(XY)\bar{Z}$ ) polarization geometry. Figure 4a,b shows the two polarized Raman spectra for a selected  $WSe_2$  pyramid cluster.

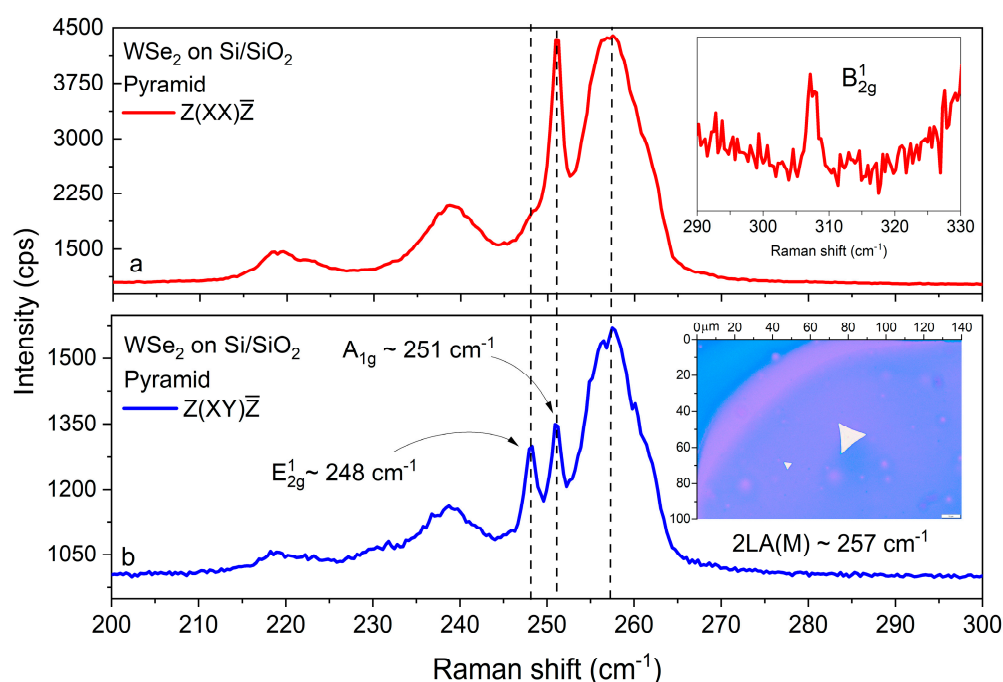


**Figure 4.** Raman characterization of  $WSe_2$  on Si/SiO<sub>2</sub>: (a) parallel- and (b) cross-polarized Raman spectra of a pyramidal  $WSe_2$  domain, with main peaks identification and an enlarged view (inset (a)) of  $B_{2g}^1$ . Inset (b): optical image of the studied pyramidal cluster.

We observed the  $E_{2g}$  peak at  $\sim 248\text{ cm}^{-1}$ , the  $A_{1g}$  peak at  $\sim 251\text{ cm}^{-1}$ , and a redshifted 2LA(M) band close to  $\sim 257\text{ cm}^{-1}$  (see Figure 4a,b), as expected for a multilayered structure [85–88] and in accordance with the AFM results (Figure 3). Furthermore, there was a well-formed peak at  $308\text{ cm}^{-1}$ . The  $A_{1g}$  intensity exceeds that of the  $E_{2g}$  line by an order of magnitude, and its forbidden appearance in the cross-polarized spectra with an intensity comparable with that of the allowed  $E_{2g}$  peak facilitates the precise determination of the frequency distance for these modes.

### 3.2. Metatungstate Method for $WSe_2$ Deposition on Fused Silica

The  $WSe_2$  produced via metatungstate deposition on fused silica formed different complex structures. An optical microscopy gallery of the different formations is presented in Figure 5a–c. The majority of the clusters had circular/oval shapes with lateral size ranging within  $10\text{--}15\text{ }\mu\text{m}$  and a relatively dense and homogeneous distribution (Figure 5a). There were also areas where highly crystalline equilateral domains with a smaller size ( $\sim 5\text{--}10\text{ }\mu\text{m}$ ) formed (Figure 5b). In addition, we observed more sophisticated patterns, usually labeled as TMDC fractal and “kirigami” shapes [75,89], such as hollow pyramids, spiral and dent rings, and propellers (Figure 5c enlarged) with both AA(A-) and AB(A-) symmetric layer stacking arrangements [90]. This complexity shows that cluster nucleation is probably affected by a broad set of factors, such as the local structural disorder of the substrate and irregular precursor accumulation [19] with variations in the W/Se stoichiometric ratio. We

can also consider possible re-evaporation [91] and chemically driven etching effects during the CVD process [92].

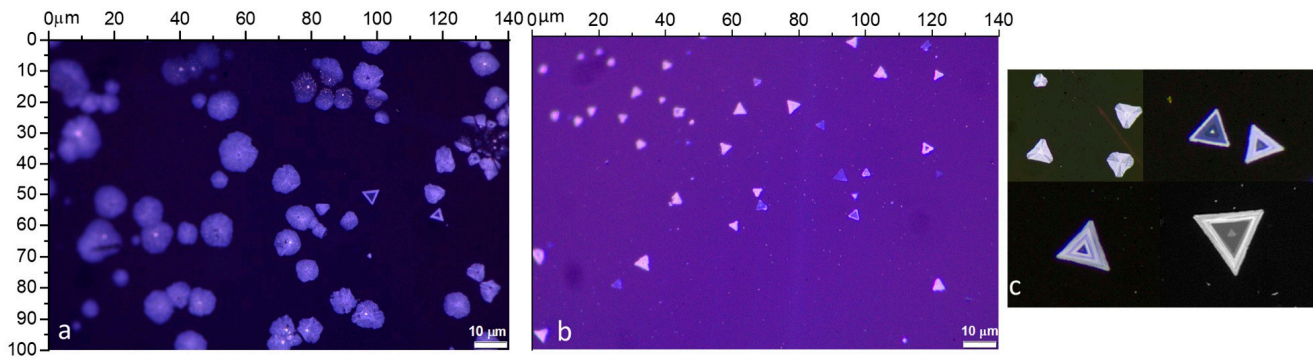


**Figure 5.** Optical images of  $\text{WSe}_2$  on fused silica under reflected illumination and  $100\times$  magnification of the dominant cluster forms (a), symmetrical triangular and ring structures (b), and an enlarged view of kirigami-type “ring” and “propeller”  $\text{WSe}_2$  structures (c).

For selected triangular  $\text{WSe}_2$  clusters on fused silica, AFM images and topographic profiles are shown in Figure 6a–f. In order to express the morphological formations and growth relief in sharper contrast, 2D maps of the AFM height and tapping mode phase variations are also presented.

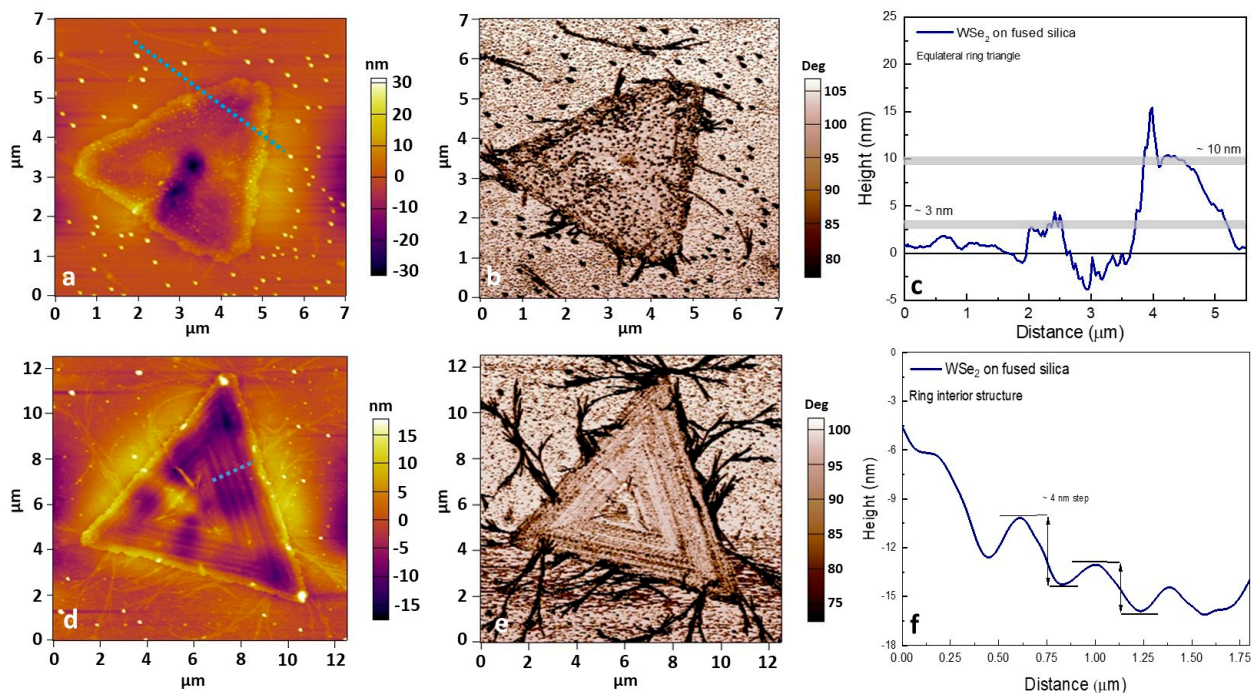


**Figure 6.** AFM (a–f) height and phase retrace maps for  $\text{WSe}_2$  on fused silica, thickness profiles of selected triangular flakes, and the complex step-like internal relief of the  $\text{WSe}_2$  “rings”.

The AC-mode phase shifts are related to the viscoelastic mechanical properties and allow us to differentiate the deposited TMDC layers from the substrate. The thickness profile identifies  $\sim 3$ – $10$  nm multilayered equilateral  $\text{WSe}_2$  with observed inner concavities, probably due to the corrosive reaction [54] between the molten precursor and the silica oxide substrate during VLS crystallization (similar to that for  $\text{Si}/\text{SiO}_2$ ). The complexity of the  $\text{WSe}_2$  ring dent structure is also revealed by  $\sim 3$ – $4$  nm step-like formations in the interior (Figure 6f).

The cross- and parallel-polarization Raman spectra of WSe<sub>2</sub> on fused silica are presented in Figure 7a–d for two selected triangular clusters: a flat one (left panel) and one with a supposed step-like ring structure (right panel).

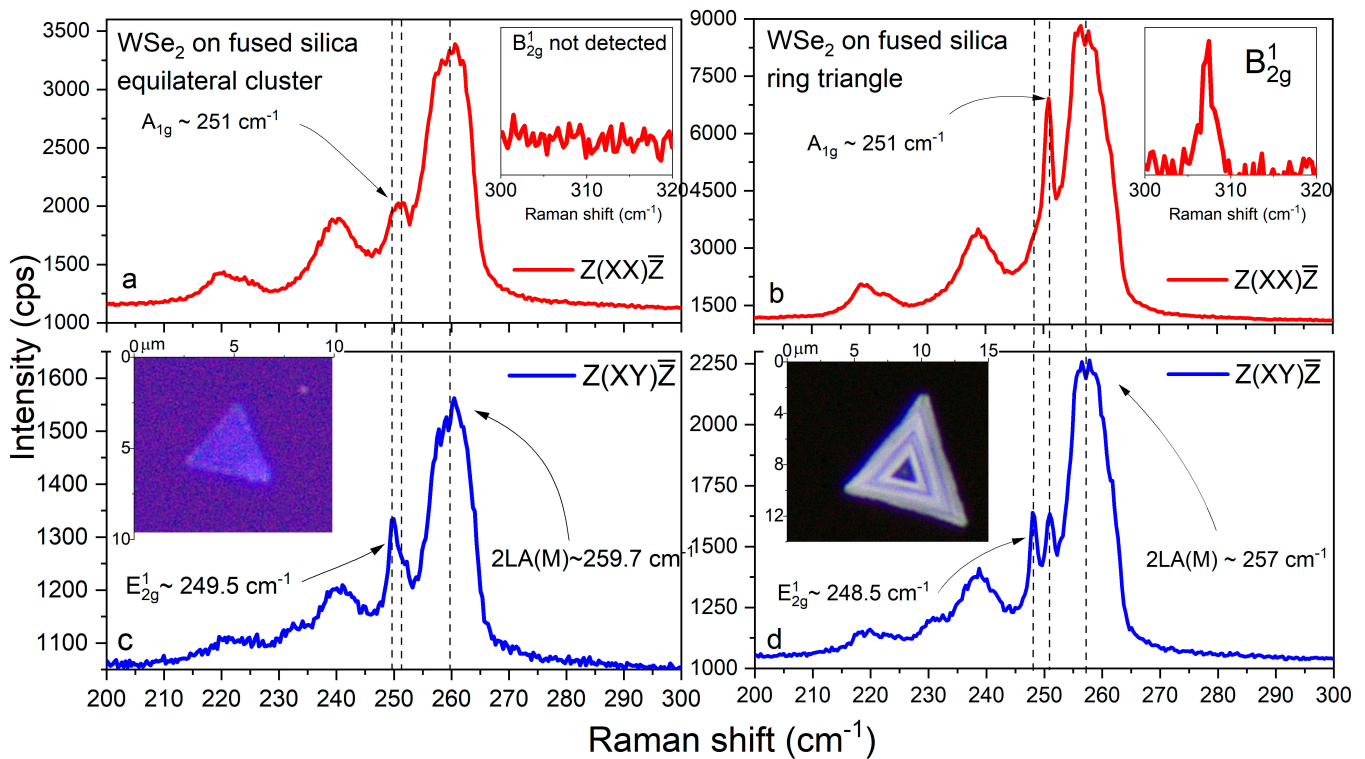


**Figure 7.** Cross- and parallel-polarized Raman spectra (a–d) of mono- and multilayer WSe<sub>2</sub> clusters on fused silica. Insets: optical images of investigated WSe<sub>2</sub> domains.

The  $E_{2g}-A_{1g}$  distance for the flat cluster amounts to  $1.5 \text{ cm}^{-1}$ , the 2LA(M) band is centered near  $260 \text{ cm}^{-1}$ , and no peak was detected near  $308 \text{ cm}^{-1}$ . This implies that the flat cluster consists of monolayer and bilayer regions. The mode positions for the ring cluster ( $E_{2g}$  at  $248.5 \text{ cm}^{-1}$ ,  $A_{1g}$  at  $251 \text{ cm}^{-1}$ , and 2LA(M) at  $\sim 257 \text{ cm}^{-1}$ ) evidence a significantly greater thickness, additionally confirmed by the presence of the forbidden  $B_{2g}^1$  peak around  $308 \text{ cm}^{-1}$  [85,86,88,93].

### 3.3. Metatungstate Method for WSe<sub>2</sub> Deposition on Sapphire

The growth of WSe<sub>2</sub> on sapphire also led to a rich set of cluster geometries and sizes, presented in Figure 8a–c. In this case, large polygonal formations with “saw-tooth” [91] edges were observed (Figure 8a). Their lateral size reached dozens of micrometers, and the domains comprised numerous multilayered bulk islands, possibly induced by singular nucleation sites. On the microscale, individual triangular flakes were also observed (Figure 8b), together with larger polygonal formations. Their equilateral geometry usually marks a highly crystalline structure with a relative lateral size of  $10 \mu\text{m}$ . Like in the case of Si/SiO<sub>2</sub>, on sapphire substrate, pyramidal structures that were  $10\text{--}40 \mu\text{m}$  in size with a typical faceted morphology were observed (Figure 8c). This particular growth is probably mediated by localized vertical precursor accumulations [49] or substrate defects that act as seeding centers [94]. The rounded edges of the peripheral layer also usually develop because of an irregular precursor distribution during WSe<sub>2</sub> formation. The DF illumination (enlarged inset image) demonstrates intensive light-scattering effects from the pyramid walls. As noted, such 3D TMDC nanoarchitectures show extreme optical second and third harmonic generation with the potential for non-linear photonic applications [82].

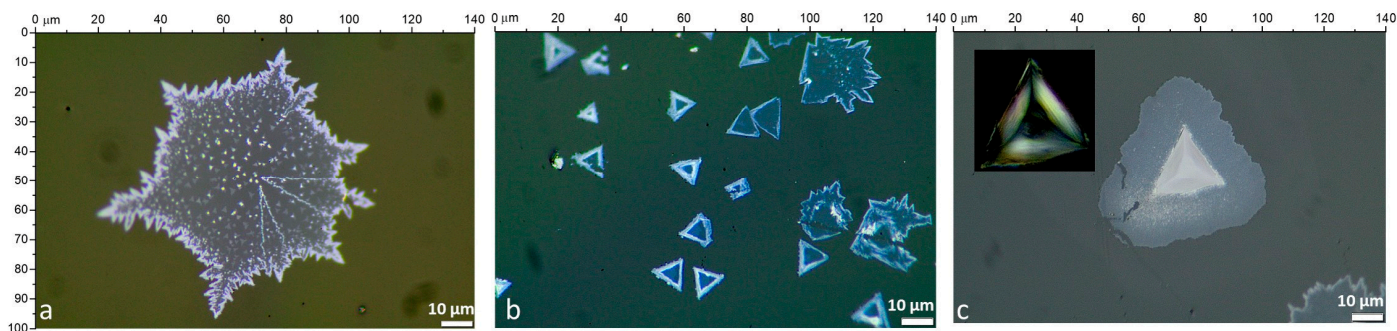


**Figure 8.** Optical images of WSe<sub>2</sub> on sapphire (under reflected light and  $\times 100$  magnification) showing (a) formations with the largest lateral size, (b) equilateral triangular clusters, and (c) pyramidal clusters of WSe<sub>2</sub> with DF illumination (inset).

AFM scan maps of a selected cluster are presented in Figure 9a–c. We determined the topographic profile of one selected equilateral triangular WSe<sub>2</sub> ( $\sim 10 \mu\text{m}$ ) cluster. To express the flake/substrate differences, the nanometer topological gradient map (a) and an AFM phase contrast image (b) are also presented.

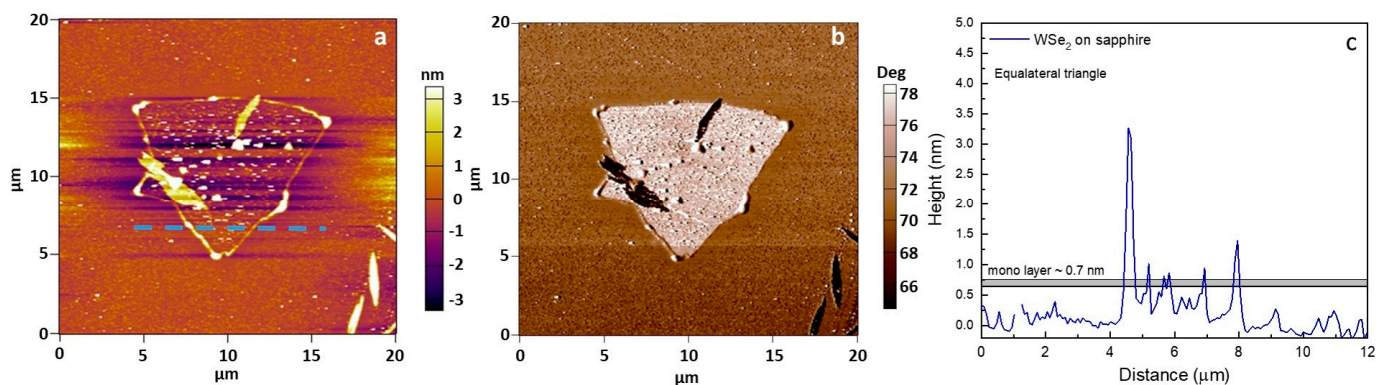


**Figure 9.** AFM height (a) and phase retrace (b) 2D maps for WSe<sub>2</sub> on sapphire with the thickness profile (c) of the monolayer cluster.

The topographic profile in Figure 9c marks a cluster thickness of  $\sim 0.7 \text{ nm}$ , close to that expected for a WSe<sub>2</sub> monolayer [16]. The observed height increase (a few nanometers) is possibly related to multilayer formation at the edges as a consequence of inhomogeneous extra precursor at the faceted domain borders [95]. Alternatively, this could also be affected by the particular substrate morphology and localized defects [30,31]. The edge area feature was identified for all observed clusters (Figure 9a,b).

The polarized Raman spectra for selected mono- and multilayer WSe<sub>2</sub> clusters on sapphire are presented in Figure 10a–d. In the former case, the virtually identical spectral positions of the E<sub>2g</sub> ( $\sim 249.7 \text{ cm}^{-1}$ ) and A<sub>1g</sub> ( $\sim 249.8 \text{ cm}^{-1}$ ) vibrational modes in the corresponding crossed and parallel polarization, the upshift of the 2LA(M) band above  $260 \text{ cm}^{-1}$ , and the absence of a B<sub>2g</sub><sup>1</sup> peak unambiguously indicate that the cluster thickness is within the monolayer limit [85–88,93]. For the thicker cluster, the expected larger separation between E<sub>2g</sub> ( $\sim 249 \text{ cm}^{-1}$ ) and A<sub>1g</sub> ( $\sim 251 \text{ cm}^{-1}$ ) was observed, together with a small redshift of 2LA(M) ( $\sim 258 \text{ cm}^{-1}$ ) and a discernible B<sub>2g</sub><sup>1</sup> peak close to  $308 \text{ cm}^{-1}$ . Still, these data imply a relatively thin, few-layered structure in contrast to the thicker multilayered clusters, for which the Raman data are shown in Figure 4a,b and 7a,b. Note the typical sharp peak structure of the main modes (as well as for Si/SiO<sub>2</sub> and fused silica), which is characteristic of objects with a high quality of crystalline ordering.

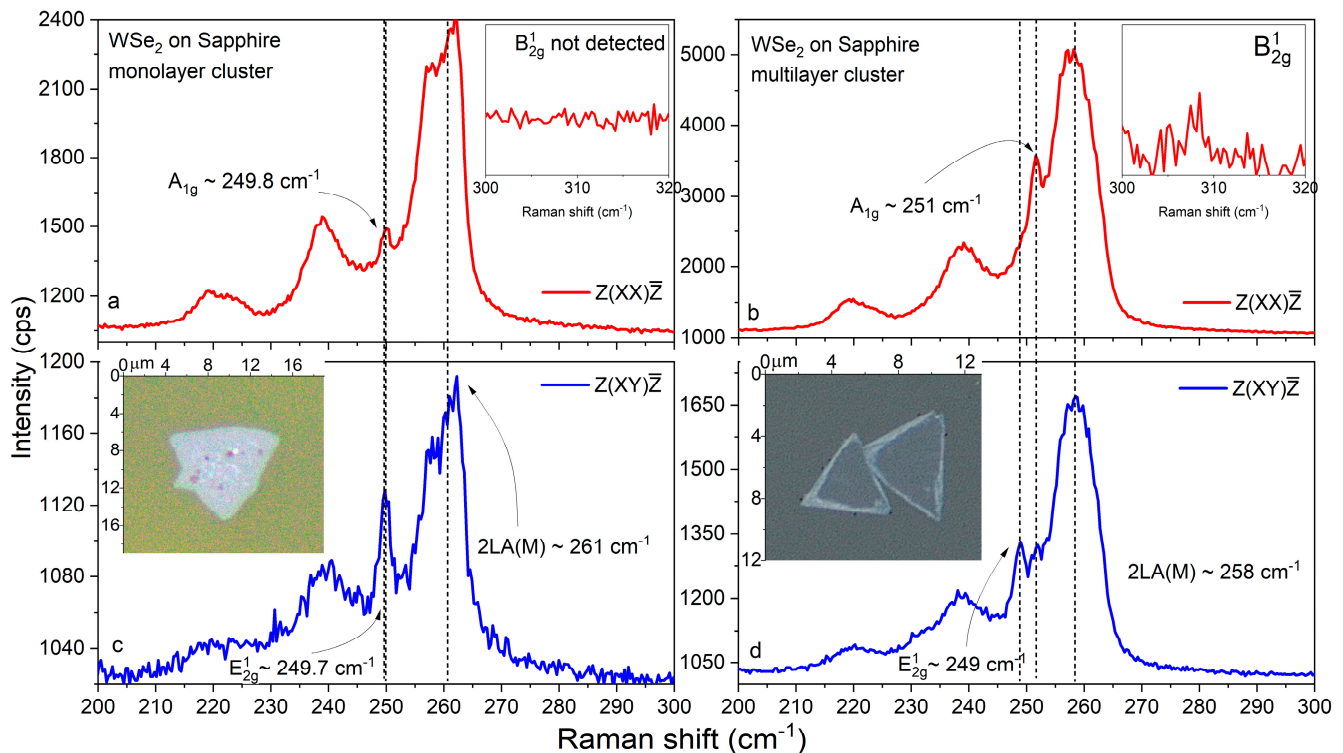


**Figure 10.** Cross- and parallel-polarized Raman spectra (a–d) of mono- and multilayer WSe<sub>2</sub> clusters on sapphire. Insets: optical images of the investigated WSe<sub>2</sub> domains.

The Raman spectrum and, specifically, the out-of-plane mode  $A_{1g}$ , are very susceptible to possible doping effects, for instance, due to plausible Na inclusions (from sodium cholate) [96]. However, the spectral data for all samples on Si/SiO<sub>2</sub>, sapphire, and fused silica substrates fit the peak positions indicative of pure WSe<sub>2</sub>.

#### 4. General Remarks

Overall, the presented data regarding the variety of WSe<sub>2</sub> clusters in terms of their size, thickness, and shape illustrate the significant differences associated with the studied substrates. These differences can be explained within the framework of the vapor–liquid–solid phenomenological model [33,64–68], where the growth mechanism is dependent on the eutectic vapor–liquid and liquid–solid interfaces. Importantly, the interfacial free energy of the molten W precursor nucleus specific for the particular substrate (Si/SiO<sub>2</sub>, fused silica, or sapphire) determines its contact area and the volume profile of the grown nanocluster.

The eutectic intermediates [49,62] formed by the fusion of WO<sub>3</sub> and alkali metal complexes (the final products of thermal decomposition of the metatungstate and the cholate promoter) strongly affect the growth kinetics. More precisely, the lowered melting point of the mixture facilitates thermodynamically favorable edge expansion on the substrate and aggregation into larger clusters. This is followed by crystallization into multilayer (vertical) or monolayer (lateral) clusters, also depending on the interfacial free energy [49]. The final WSe<sub>2</sub> formation stages with chemical conversion are determined by Se super-saturation and dissolution into the molten WO<sub>3</sub>/alkali metal mixture [49] and hydrogen-induced reduction.

The simultaneous formation of monolayer and multilayer WSe<sub>2</sub> (observed in the case of the sapphire substrate) and, especially, the presence of more composite clusters fractions can be ascribed to localized perturbations in the above growth process under a number of concurrent factors. This random morphological variation was observed for all substrate types. Nucleation into self-assembled multilayer structures could be caused by precursor accumulation and/or substrate defects acting as seed centers, promoting

multilayer growth (pyramidal formations). Deviations from the highly crystalline triangular geometry can be associated with local stoichiometric imbalance (propeller flakes) and/or etching and substrate corrosion effects (for Si/SiO<sub>2</sub> and fused silica) creating numerous ring dent clusters.

Another important factor is the adsorption effect of the precursors, utilized by the sodium cholate hydrate. The purpose of the surfactant seed promoter is to provide favorable heterogeneous nucleation sites. This is correspondingly determined by the interaction and anchoring of its polar (hydrophilic) and nonpolar (hydrophobic) parts with the precursor solvent and the substrate surface [52,54,61]. However, the intensity of these interactions depends on the different adhesive energies of the particular substrate materials and also influences the consequent CVD multilayer/monolayer formation process of WSe<sub>2</sub>. In this context, further optimization of the method is required to allow for precise thickness control and uniform planar growth. Nevertheless, it shows opportunities for the synthesis and engineering of TMDC structures with particular forms and applications. Based on the unique excitonic [10] and spintronic [12] characteristics of monolayer WSe<sub>2</sub>, together with the valleytronic [97] and memristive [98] functionalities of multilayered structures, the implemented liquid precursor-mediated CVD approach opens up many practical possibilities.

The presented variety of Raman spectra resulting from the challenging mono- and multilayered morphology of the WSe<sub>2</sub> formations reveals the informative capabilities of polarized Raman spectroscopy for the analysis of TMDC. This is well demonstrated by tracking the spectral behavior (frequency shifts and intensity change) of the fundamental A<sub>1g</sub> and E<sub>2g</sub> vibration modes together with the second-order 2LA(M) and the occasional presence of forbidden B<sub>2g</sub><sup>1</sup> peaks, exploiting their high sensitivity to the layer number. In addition, the spectral parameters of the A<sub>1g</sub> and E<sub>2g</sub> Raman lines, such as the FWHM (full width of half-maximum) and their distance and intensity ratio, are summarized in Table 1 for all studied clusters.

**Table 1.** Raman line characteristics for the studied WSe<sub>2</sub> clusters: FWHM and peak intensity ratio calculated by Voigt fitting.

	WSe <sub>2</sub> Pyramidal on Si/SiO <sub>2</sub>	WSe <sub>2</sub> Mono (Bi-) Layer on Fused Silica	WSe <sub>2</sub> Multilayer on Fused Silica	WSe <sub>2</sub> Monolayer on Sapphire	WSe <sub>2</sub> Multilayer on Sapphire
E <sub>2g</sub> FWHM (cm <sup>-1</sup> )	2	2.2	2	2.5	2.3
A <sub>1g</sub> FWHM (cm <sup>-1</sup> )	1.5	2	2	2.5	2.3
E <sub>2g</sub> -A <sub>1g</sub> distance (cm <sup>-1</sup> )	3	1.5	2.5	≈0	2
I(A <sub>1g</sub> )/I(E <sub>2g</sub> )	9.5	2.5	11	2.3	9

Our data are in very good agreement with the corresponding numerical values and trends presented in the pioneering work of Zhao et al. [88]. The slightly larger A<sub>1g</sub> and E<sub>2g</sub> linewidths in our spectra can be explained by the difference in growth methods. Our WSe<sub>2</sub> clusters were obtained by means of direct CVD synthesis, similar to that used for the deposition of continuous layers, while the polarized Raman analysis in Ref. [88] was performed on exfoliated flakes from WSe<sub>2</sub> crystals grown by means of chemical vapor transport.

## 5. Conclusions

In conclusion, we investigated the growth prospects for multi- and monolayer WSe<sub>2</sub> formation (on Si/SiO<sub>2</sub>, fused silica, and sapphire substrates) using a facile CVD method based on the utilization of an ammonium metatungstate precursor and sodium cholate as

a growth promoter. WSe<sub>2</sub> synthesis was achieved via a simple preparation procedure at moderate working temperatures (~710 °C) and ambient pressure.

Various WSe<sub>2</sub> formations with different sizes, layer numbers, and structures were observed and characterized via optical microscopy, AFM, and polarized Raman spectroscopy. It was shown that under the applied synthesis conditions, the metatungstate/cholate method resulted in the formation of both monolayer and multilayer WSe<sub>2</sub> clusters.

A comprehensive polarized Raman analysis to accurately identify the first-(A<sub>1g</sub> and E<sub>2g</sub>) and second-order (2LA(M)) vibrational modes enabled us to obtain a reliable semi-quantitative estimate of the WSe<sub>2</sub> thickness for the variety of WSe<sub>2</sub> structures observed on the different substrates.

A higher distribution density and coverage of the synthesized flakes were observed in the case of fused silica and sapphire. For sapphire, the maximal lateral size of the WSe<sub>2</sub> flakes reached hundreds of micrometers. Meanwhile, in the case of Si/SiO<sub>2</sub>, most of the clusters were scattered pyramidal forms with heights of up to ~100 nm and lateral sizes of tens of micrometers. The presented results provide a base for further development of this simplistic metatungstate synthesis method towards improved growth control and reproducibility.

**Author Contributions:** Conceptualization, K.B., P.R., V.M. and D.D.; methodology, K.B., P.R., N.M., V.V., V.S., T.L., D.D. and V.M.; software, K.B.; validation, K.B. and P.R.; formal analysis, K.B. and P.R.; investigation, K.B., P.R., N.M., V.V., V.S., T.L., D.D. and V.M.; resources, D.D., V.M. and P.R.; data curation, K.B.; writing—original draft preparation, K.B.; writing—review and editing, K.B., V.M., D.D. and P.R.; visualization, K.B.; supervision, D.D. and V.M.; project administration, D.D. and V.M.; funding acquisition, D.D. and V.M. All authors have read and agreed to the published version of the manuscript.

**Funding:** The authors gratefully acknowledge the financial support provided by the Bulgarian Science Fund under the grant numbers DFNI KII-06-ДО 02/2 and DFNI KII-06-ДО 02/3 within the framework of the M-ERA program project “Functional 2D materials and heterostructures for hybrid spintronic memristive devices”. Research equipment of the Distributed Research Infrastructure INFRAMAT, part of the Bulgarian National Roadmap for Research Infrastructures and supported by Bulgarian Ministry of Education and Science, was used in this investigation.

**Data Availability Statement:** The data presented in this study are available on request from the corresponding author.

**Acknowledgments:** N.M., V.M., and P.R. acknowledge financial support from the European Regional Development Fund within the Operational Programme “Science and Education for Smart Growth 2014–2020” under the Project CoE “National Center of Mechatronics and Clean Technologies” BG05M2OP001-1.001-0008-C01.

**Conflicts of Interest:** The authors declare no conflicts of interest.

## References

1. Mohl, M.; Rautio, A.-R.; Asres, G.A.; Wasala, M.; Patil, P.D.; Talapatra, S.; Kordas, K. 2D Tungsten Chalcogenides: Synthesis, Properties and Applications. *Adv. Mater. Interfaces* **2020**, *7*, 2000002. [[CrossRef](#)]
2. Eftekhari, A. Tungsten dichalcogenides (WS<sub>2</sub>, WSe<sub>2</sub>, and WTe<sub>2</sub>): Materials chemistry and applications. *J. Mater. Chem. A* **2017**, *5*, 18299–18325. [[CrossRef](#)]
3. Cheng, Q.; Pang, J.J.; Sun, D.; Wang, J.J.; Zhang, S.; Liu, F.; Chen, Y.; Yang, R.; Liang, N.; Lu, X.; et al. WSe<sub>2</sub> 2D p-type semiconductor-based electronic devices for information technology: Design, preparation, and applications. *InfoMat* **2020**, *2*, 656–697. [[CrossRef](#)]
4. Yao, Z.; Liu, J.; Xu, K.; Chow, E.K.C.C.; Zhu, W. Material Synthesis and Device Aspects of Monolayer Tungsten Diselenide. *Sci. Rep.* **2018**, *8*, 5221. [[CrossRef](#)] [[PubMed](#)]
5. Zhou, J.; Lin, J.; Huang, X.; Zhou, Y.; Chen, Y.; Xia, J.; Wang, H.; Xie, Y.; Yu, H.; Lei, J.; et al. A library of atomically thin metal chalcogenides. *Nature* **2018**, *556*, 355–359. [[CrossRef](#)] [[PubMed](#)]
6. Xu, S.; Shen, J.; Long, G.; Wu, Z.; Bao, Z.Q.; Liu, C.C.; Xiao, X.; Han, T.; Lin, J.; Wu, Y.; et al. Odd-Integer Quantum Hall States and Giant Spin Susceptibility in p-type Few-Layer WSe<sub>2</sub>. *Phys. Rev. Lett.* **2017**, *118*, 067702. [[CrossRef](#)]
7. Wang, J.; Xie, F.; Cao, X.H.; An, S.C.; Zhou, W.X.; Tang, L.M.; Chen, K.Q. Excellent Thermoelectric Properties in monolayer WSe<sub>2</sub> Nanoribbons due to Ultralow Phonon Thermal Conductivity. *Sci. Rep.* **2017**, *7*, 41418. [[CrossRef](#)]

8. Desai, S.B.; Seol, G.; Kang, J.S.; Fang, H.; Battaglia, C.; Kapadia, R.; Ager, J.W.; Guo, J.; Javey, A. Strain-induced indirect to direct bandgap transition in multilayer WSe<sub>2</sub>. *Nano Lett.* **2014**, *14*, 4592–4597. [[CrossRef](#)]
9. Zhao, W.; Ghorannevis, Z.; Chu, L.; Toh, M.; Kloc, C.; Tan, P.H.; Eda, G. Evolution of electronic structure in atomically thin sheets of WS<sub>2</sub> and WSe<sub>2</sub>. *ACS Nano* **2013**, *7*, 791–797. [[CrossRef](#)]
10. Courtade, E.; Semina, M.; Manca, M.; Glazov, M.M.; Robert, C.; Cadiz, F.; Wang, G.; Taniguchi, T.; Watanabe, K.; Pierre, M.; et al. Charged excitons in monolayer WSe<sub>2</sub>: Experiment and theory. *Phys. Rev. B Condens. Matter Mater. Phys.* **2017**, *96*, 085302. [[CrossRef](#)]
11. Robert, C. When bright and dark bind together. *Nat. Nanotechnol.* **2018**, *13*, 982–983. [[CrossRef](#)]
12. Sierra, J.F.; Fabian, J.; Kawakami, R.K.; Roche, S.; Valenzuela, S.O. Van der Waals heterostructures for spintronics and opto-spintronics. *Nat. Nanotechnol.* **2021**, *16*, 856–868. [[CrossRef](#)]
13. Zhao, S.; Li, X.; Dong, B.; Wang, H.; Wang, H.; Zhang, Y.; Han, Z.; Zhang, H. Valley manipulation in monolayer transition metal dichalcogenides and their hybrid systems: Status and challenges. *Rep. Prog. Phys.* **2021**, *84*, 026401. [[CrossRef](#)]
14. Cai, Z.; Liu, B.; Zou, X.; Cheng, H.M. Chemical Vapor Deposition Growth and Applications of Two-Dimensional Materials and Their Heterostructures. *Chem. Rev.* **2018**, *118*, 6091–6133. [[CrossRef](#)]
15. Tang, L.; Tan, J.; Nong, H.; Liu, B.; Cheng, H.-M. Chemical Vapor Deposition Growth of Two-Dimensional Compound Materials: Controllability, Material Quality, and Growth Mechanism. *Acc. Mater. Res.* **2020**, *2*, 36–47. [[CrossRef](#)]
16. Liu, J.; Zeng, M.; Wang, L.; Chen, Y.; Xing, Z.; Zhang, T.; Liu, Z.; Zuo, J.; Nan, F.; Mendes, R.G.; et al. Ultrafast Self-Limited Growth of Strictly Monolayer WSe<sub>2</sub> Crystals. *Small* **2016**, *12*, 5741–5749. [[CrossRef](#)]
17. Zhang, L.; Dong, J.; Ding, F. Strategies, Status, and Challenges in Wafer Scale Single Crystalline Two-Dimensional Materials Synthesis. *Chem. Rev.* **2021**, *121*, 6321–6372. [[CrossRef](#)] [[PubMed](#)]
18. Hoang, A.T.; Qu, K.; Chen, X.; Ahn, J.H. Large-area synthesis of transition metal dichalcogenides via CVD and solution-based approaches and their device applications. *Nanoscale* **2021**, *13*, 615–633. [[CrossRef](#)] [[PubMed](#)]
19. Jung, Y.; Ji, E.; Capasso, A.; Lee, G.-H.H. Recent Progresses in the Growth of Two-dimensional Transition Metal Dichalcogenides. *J. Korean Ceram. Soc.* **2019**, *56*, 24–36. [[CrossRef](#)]
20. Brent, J.R.; Savjani, N.; O'Brien, P. Synthetic approaches to two-dimensional transition metal dichalcogenide nanosheets. *Prog. Mater. Sci.* **2017**, *89*, 411–478. [[CrossRef](#)]
21. Han, J.H.; Kwak, M.; Kim, Y.; Cheon, J. Recent Advances in the Solution-Based Preparation of Two-Dimensional Layered Transition Metal Chalcogenide Nanostructures. *Chem. Rev.* **2018**, *118*, 6151–6188. [[CrossRef](#)]
22. Xie, C.; Yang, P.; Huan, Y.; Cui, F.; Zhang, Y. Roles of salts in the chemical vapor deposition synthesis of two-dimensional transition metal chalcogenides. *Dalt. Trans.* **2020**, *49*, 10319–10327. [[CrossRef](#)]
23. Wong, S.L.; Liu, H.; Chi, D. Recent progress in chemical vapor deposition growth of two-dimensional transition metal dichalcogenides. *Prog. Cryst. Growth Charact. Mater.* **2016**, *62*, 9–28. [[CrossRef](#)]
24. You, J.; Hossain, M.D.; Luo, Z. Synthesis of 2D transition metal dichalcogenides by chemical vapor deposition with controlled layer number and morphology. *Nano Converg.* **2018**, *5*, 26. [[CrossRef](#)]
25. Li, S. Salt-assisted chemical vapor deposition of two-dimensional transition metal dichalcogenides. *iScience* **2021**, *24*, 103229. [[CrossRef](#)]
26. Bosi, M. Growth and synthesis of mono and few-layers transition metal dichalcogenides by vapour techniques: A review. *RSC Adv.* **2015**, *5*, 75500–75518. [[CrossRef](#)]
27. Lan, S.; Zhang, Z.; Hong, Y.; She, Y.; Pan, B.; Xu, Y.; Wang, P. Judicious Selection of Precursors with Suitable Chemical Valence State for Controlled Growth of Transition Metal Chalcogenides. *Adv. Mater. Interfaces* **2023**, *10*, 2300713. [[CrossRef](#)]
28. Alahmadi, M.; Mahvash, F.; Szkopek, T.; Siaj, M. A two-step chemical vapor deposition process for the growth of continuous vertical heterostructure WSe<sub>2</sub>/h-BN and its optical properties. *RSC Adv.* **2021**, *11*, 16962–16969. [[CrossRef](#)]
29. Zhang, X.; Choudhury, T.H.; Chubarov, M.; Xiang, Y.; Jariwala, B.; Zhang, F.; Alem, N.; Wang, G.C.; Robinson, J.A.; Redwing, J.M. Diffusion-Controlled Epitaxy of Large Area Coalesced WSe<sub>2</sub> Monolayers on Sapphire. *Nano Lett.* **2018**, *18*, 1049–1056. [[CrossRef](#)] [[PubMed](#)]
30. Han, A.; Aljarb, A.; Liu, S.; Li, P.; Ma, C.; Xue, F.; Lopatin, S.; Yang, C.W.; Huang, J.K.; Wan, Y.; et al. Growth of 2H stacked WSe<sub>2</sub> bilayers on sapphire. *Nanoscale Horiz.* **2019**, *4*, 1434–1442. [[CrossRef](#)]
31. Chen, L.; Liu, B.; Ge, M.; Ma, Y.; Abbas, A.N.; Zhou, C. Step-Edge-Guided Nucleation and Growth of Aligned WSe<sub>2</sub> on Sapphire via a Layer-over-Layer Growth Mode. *ACS Nano* **2015**, *9*, 8368–8375. [[CrossRef](#)] [[PubMed](#)]
32. Kim, H.; Ahn, G.H.; Cho, J.; Amani, M.; Mastandrea, J.P.; Groschner, C.K.; Lien, D.H.; Zhao, Y.; Ager, J.W.; Scott, M.C.; et al. Synthetic WSe<sub>2</sub> monolayers with high photoluminescence quantum yield. *Sci. Adv.* **2019**, *5*, eaau4728. [[CrossRef](#)] [[PubMed](#)]
33. Rasouli, H.R.; Mehmood, N.; Çakiroğlu, O.; Serkan Kasirga, T. Real time optical observation and control of atomically thin transition metal dichalcogenide synthesis. *Nanoscale* **2019**, *11*, 7317–7323. [[CrossRef](#)] [[PubMed](#)]
34. Naylor, C.H.; Parkin, W.M.; Gao, Z.; Kang, H.; Noyan, M.; Wexler, R.B.; Tan, L.Z.; Kim, Y.; Kehayias, C.E.; Streller, F.; et al. Large-area synthesis of high-quality monolayer 1T'-WTe<sub>2</sub> flakes. *2D Mater.* **2017**, *4*, 021008. [[CrossRef](#)] [[PubMed](#)]
35. Mandyam, S.V.; Zhao, M.Q.; Masih Das, P.; Zhang, Q.; Price, C.C.; Gao, Z.; Shenoy, V.B.; Drndić, M.; Johnson, A.T.C. Controlled Growth of Large-Area Bilayer Tungsten Diselenides with Lateral P-N Junctions. *ACS Nano* **2019**, *13*, 10490–10498. [[CrossRef](#)] [[PubMed](#)]

36. Fan, S.; Joon Yun, S.; Jong Yu, W.; Hee Lee, Y.; Fan, S.; Yun, S.J.; Lee, Y.H.; Yu, W.J. Tailoring Quantum Tunneling in a Vanadium-Doped WSe<sub>2</sub>/SnSe<sub>2</sub> Heterostructure. *Adv. Sci.* **2020**, *7*, 1902751. [[CrossRef](#)]
37. Joon Yun, S.; Loc Duong, D.; Manh Ha, D.; Singh, K.; Luan Phan, T.; Choi, W.; Kim, Y.-M.; Hee Lee, Y.; Yun, S.J.; Duong, D.L.; et al. Ferromagnetic Order at Room Temperature in Monolayer WSe<sub>2</sub> Semiconductor via Vanadium Dopant. *Adv. Sci.* **2020**, *7*, 1903076. [[CrossRef](#)]
38. Duong, D.L.; Yun, S.J.; Kim, Y.; Kim, S.G.; Lee, Y.H. Long-range ferromagnetic ordering in vanadium-doped WSe<sub>2</sub> semiconductor. *Appl. Phys. Lett.* **2019**, *115*, 242406. [[CrossRef](#)]
39. Zhang, F.; Zheng, B.; Sebastian, A.; Olson, D.H.; Liu, M.; Fujisawa, K.; Pham, Y.T.H.; Jimenez, V.O.; Kalappattil, V.; Miao, L.; et al. Monolayer Vanadium-Doped Tungsten Disulfide: A Room-Temperature Dilute Magnetic Semiconductor. *Adv. Sci.* **2020**, *7*, 2001174. [[CrossRef](#)] [[PubMed](#)]
40. Ortiz Jimenez, V.; Pham, Y.T.H.; Liu, M.; Zhang, F.; Yu, Z.; Kalappattil, V.; Muchharla, B.; Eggers, T.; Duong, D.L.; Terrones, M.; et al. Light-Controlled Room Temperature Ferromagnetism in Vanadium-Doped Tungsten Disulfide Semiconducting Monolayers. *Adv. Electron. Mater.* **2021**, *7*, 2100030. [[CrossRef](#)]
41. Han, G.H.; Kybert, N.J.; Naylor, C.H.; Lee, B.S.; Ping, J.; Park, J.H.; Kang, J.; Lee, S.Y.; Lee, Y.H.; Agarwal, R.; et al. Seeded growth of highly crystalline molybdenum disulphide monolayers at controlled locations. *Nat. Commun.* **2015**, *6*, 6128. [[CrossRef](#)]
42. Naylor, C.H.; Parkin, W.M.; Ping, J.; Gao, Z.; Zhou, Y.R.; Kim, Y.; Streller, F.; Carpick, R.W.; Rappe, A.M.; Drndić, M.; et al. Monolayer single-crystal 1T'-MoTe<sub>2</sub> grown by chemical vapor deposition exhibits weak antilocalization effect. *Nano Lett.* **2016**, *16*, 4297–4304. [[CrossRef](#)] [[PubMed](#)]
43. Zuo, Y.; Yu, W.; Liu, C.; Cheng, X.; Qiao, R.; Liang, J.; Zhou, X.; Wang, J.; Wu, M.; Zhao, Y.; et al. Optical fibres with embedded two-dimensional materials for ultrahigh nonlinearity. *Nat. Nanotechnol.* **2020**, *15*, 987–991. [[CrossRef](#)]
44. Guan, H.; Zhao, B.; Zhao, W.; Ni, Z. Liquid-precursor-intermediated synthesis of atomically thin transition metal dichalcogenides. *Mater. Horiz.* **2023**, *10*, 1105–1120. [[CrossRef](#)] [[PubMed](#)]
45. Ouyang, D.; Tong, X.; Liu, S.; Wang, J.; Zhao, Y.; Liu, R.; Zhao, X.; Zhang, N.; Cao, F.; Liu, Y.; et al. Superior Nonlinear Optical Response in Non-Centrosymmetric Stacking Edge-Rich Spiral MoTe<sub>2</sub> Nanopyramids. *Adv. Funct. Mater.* **2022**, *32*, 2113052. [[CrossRef](#)]
46. Lee, E.; Kim, J.; Yun, S.J.; Kim, Y. Near-field visualization of charge transfer at MoSe<sub>2</sub>/WSe<sub>2</sub> lateral heterojunction. *Opt. Mater. Express* **2019**, *9*, 1864–1871. [[CrossRef](#)]
47. Zhang, T.; Fujisawa, K.; Zhang, F.; Liu, M.; Lucking, M.C.; Gontijo, R.N.; Lei, Y.; Liu, H.; Crust, K.; Granzier-Nakajima, T.; et al. Universal In Situ Substitutional Doping of Transition Metal Dichalcogenides by Liquid-Phase Precursor-Assisted Synthesis. *ACS Nano* **2020**, *14*, 4326–4335. [[CrossRef](#)]
48. Wan, X.; Miao, X.; Yao, J.; Wang, S.; Shao, F.; Xiao, S.; Zhan, R.; Chen, K.; Zeng, X.; Gu, X.; et al. In Situ Ultrafast and Patterned Growth of Transition Metal Dichalcogenides from Inkjet-Printed Aqueous Precursors. *Adv. Mater.* **2021**, *33*, 2100260. [[CrossRef](#)]
49. Jiang, D.; Wang, X.; Chen, R.; Sun, J.; Kang, H.; Ji, D.; Liu, Y.; Wei, D. Self-Expanding Molten Salt-Driven Growth of Patterned Transition-Metal Dichalcogenide Crystals. *J. Am. Chem. Soc.* **2022**, *144*, 8746–8755. [[CrossRef](#)]
50. Patil, B.; Bernini, C.; Marré, D.; Pellegrino, L.; Pallecchi, I. Ink-jet printing and drop-casting deposition of 2H-phase SnSe<sub>2</sub> and WSe<sub>2</sub> nanoflake assemblies for thermoelectric applications. *Nanotechnology* **2021**, *33*, 035302. [[CrossRef](#)]
51. Abbas, O.A.; Zeimpekis, I.; Wang, H.; Lewis, A.H.; Sessions, N.P.; Ebert, M.; Aspiotis, N.; Huang, C.C.; Hewak, D.; Mailis, S.; et al. Solution-Based Synthesis of Few-Layer WS<sub>2</sub> Large Area Continuous Films for Electronic Applications. *Sci. Rep.* **2020**, *10*, 1696. [[CrossRef](#)] [[PubMed](#)]
52. Ling, X.; Lee, Y.H.; Lin, Y.; Fang, W.; Yu, L.; Dresselhaus, M.S.; Kong, J. Role of the seeding promoter in MoS<sub>2</sub> growth by chemical vapor deposition. *Nano Lett.* **2014**, *14*, 464–472. [[CrossRef](#)]
53. Yun, S.J.; Han, G.H.; Kim, H.; Duong, D.L.; Shin, B.G.; Zhao, J.; Vu, Q.A.; Lee, J.; Lee, S.M.; Lee, Y.H. Telluriding monolayer MoS<sub>2</sub> and WS<sub>2</sub> via alkali metal scooter. *Nat. Commun.* **2017**, *8*, 2163. [[CrossRef](#)] [[PubMed](#)]
54. Kim, H.; Han, G.H.; Yun, S.J.; Zhao, J.; Keum, D.H.; Jeong, H.Y.; Ly, T.H.; Jin, Y.; Park, J.H.; Moon, B.H.; et al. Role of alkali metal promoter in enhancing lateral growth of monolayer transition metal dichalcogenides. *Nanotechnology* **2017**, *28*, 36LT01. [[CrossRef](#)] [[PubMed](#)]
55. Han, W.; Liu, K.; Yang, S.; Wang, F.; Su, J.; Jin, B.; Li, H.; Zhai, T. Salt-assisted chemical vapor deposition of two-dimensional materials. *Sci. China Chem.* **2019**, *62*, 1300–1311. [[CrossRef](#)]
56. Huang, L.; Hu, Z.; Jin, H.; Wu, J.; Liu, K.; Xu, Z.; Wan, J.; Zhou, H.; Duan, J.; Hu, B.; et al. Salt-Assisted Synthesis of 2D Materials. *Adv. Funct. Mater.* **2020**, *30*, 1908486. [[CrossRef](#)]
57. Li, S.; Wang, S.; Tang, D.M.; Zhao, W.; Xu, H.; Chu, L.; Bando, Y.; Golberg, D.; Eda, G. Halide-assisted atmospheric pressure growth of large WSe<sub>2</sub> and WS<sub>2</sub> monolayer crystals. *Appl. Mater. Today* **2015**, *1*, 60–66. [[CrossRef](#)]
58. Bai, X.; Li, S.; Das, S.; Du, L.; Dai, Y.; Yao, L.; Raju, R.; Du, M.; Lipsanen, H.; Sun, Z. Single-step chemical vapour deposition of anti-pyramid MoS<sub>2</sub>/WS<sub>2</sub> vertical heterostructures. *Nanoscale* **2021**, *13*, 4537–4542. [[CrossRef](#)]
59. Hunyadi, D.; Sajó, I.; Szilágyi, I.M. Structure and thermal decomposition of ammonium metatungstate. *J. Therm. Anal. Calorim.* **2013**, *116*, 329–337. [[CrossRef](#)]
60. Griffin, A.; Nisi, K.; Pepper, J.; Harvey, A.; Szydłowska, B.M.; Coleman, J.N.; Backes, C. Effect of Surfactant Choice and Concentration on the Dimensions and Yield of Liquid-Phase-Exfoliated Nanosheets. *Chem. Mater.* **2020**, *32*, 2852–2862. [[CrossRef](#)]

61. Ko, H.; Kim, H.S.; Ramzan, M.S.; Byeon, S.; Choi, S.H.; Kim, K.K.; Kim, Y.H.; Kim, S.M. Atomistic mechanisms of seeding promoter-controlled growth of molybdenum disulphide. *2D Mater.* **2019**, *7*, 015013. [[CrossRef](#)]
62. Wang, P.; Lei, J.; Qu, J.; Cao, S.; Jiang, H.; He, M.; Shi, H.; Sun, X.; Gao, B.; Liu, W. Mechanism of Alkali Metal Compound-Promoted Growth of Monolayer MoS<sub>2</sub>: Eutectic Intermediates. *Chem. Mater.* **2019**, *31*, 873–880. [[CrossRef](#)]
63. Kim, M.; Son, M.; Seo, D.B.; Kim, J.; Jang, M.; Kim, D.I.; Lee, S.; Yim, S.; Song, W.; Myung, S.; et al. Dual Catalytic and Self-Assembled Growth of Two-Dimensional Transition Metal Dichalcogenides Through Simultaneous Predeposition Process. *Small* **2023**, *19*, 2206350. [[CrossRef](#)] [[PubMed](#)]
64. Li, S.; Lin, Y.C.; Liu, X.Y.; Hu, Z.; Wu, J.; Nakajima, H.; Liu, S.; Okazaki, T.; Chen, W.; Minari, T.; et al. Wafer-scale and deterministic patterned growth of monolayer MoS<sub>2</sub> via vapor–liquid–solid method. *Nanoscale* **2019**, *11*, 16122–16129. [[CrossRef](#)]
65. Li, S.; Lin, Y.C.; Zhao, W.; Wu, J.; Wang, Z.; Hu, Z.; Shen, Y.; Tang, D.M.; Wang, J.; Zhang, Q.; et al. Vapour–liquid–solid growth of monolayer MoS<sub>2</sub> nanoribbons. *Nat. Mater.* **2018**, *17*, 535–542. [[CrossRef](#)]
66. Cheng, Z.; He, S.; Han, X.; Wang, M.; Zhang, S.; Liu, S.; Liang, G.; Zhang, S.; Xia, M. Interfaces determine the nucleation and growth of large NbS<sub>2</sub> single crystals. *CrystEngComm* **2021**, *23*, 1312–1320. [[CrossRef](#)]
67. Qiang, X.; Iwamoto, Y.; Watanabe, A.; Kameyama, T.; He, X.; Kaneko, T.; Shibuta, Y.; Kato, T. Non-classical nucleation in vapor–liquid–solid growth of monolayer WS<sub>2</sub> revealed by in-situ monitoring chemical vapor deposition. *Sci. Rep.* **2021**, *11*, 22285. [[CrossRef](#)]
68. Li, C.; Kameyama, T.; Takahashi, T.; Kaneko, T.; Kato, T. Nucleation dynamics of single crystal WS<sub>2</sub> from droplet precursors uncovered by in-situ monitoring. *Sci. Rep.* **2019**, *9*, 12958. [[CrossRef](#)]
69. Chen, J.; Liu, B.; Liu, Y.; Tang, W.; Nai, C.T.; Li, L.; Zheng, J.; Gao, L.; Zheng, Y.; Shin, H.S.; et al. Chemical Vapor Deposition of Large-Sized Hexagonal WSe<sub>2</sub> Crystals on Dielectric Substrates. *Adv. Mater.* **2015**, *27*, 6722–6727. [[CrossRef](#)]
70. Zhu, S.; Wang, Q. A simple method for understanding the triangular growth patterns of transition metal dichalcogenide sheets. *AIP Adv.* **2015**, *5*, 107105. [[CrossRef](#)]
71. Wang, S.; Rong, Y.; Fan, Y.; Pacios, M.; Bhaskaran, H.; He, K.; Warner, J.H. Shape evolution of monolayer MoS<sub>2</sub> crystals grown by chemical vapor deposition. *Chem. Mater.* **2014**, *26*, 6371–6379. [[CrossRef](#)]
72. Momeni, K.; Ji, Y.; Zhang, K.; Robinson, J.A.; Chen, L.Q. Multiscale framework for simulation-guided growth of 2D materials. *npj 2D Mater. Appl.* **2018**, *2*, 27. [[CrossRef](#)]
73. Lv, R.; Terrones, H.; Elías, A.L.; Perea-López, N.; Gutiérrez, H.R.; Cruz-Silva, E.; Rajukumar, L.P.; Dresselhaus, M.S.; Terrones, M. Two-dimensional transition metal dichalcogenides: Clusters, ribbons, sheets and more. *Nano Today* **2015**, *10*, 559–592. [[CrossRef](#)]
74. Wang, X.; Yang, H.; Feng, H.; Wang, L.; Chen, S.; Zhou, Z.; Wang, S.; Liu, Q. Shape-dependent close-edge 2D-MoS<sub>2</sub> nanobelts. *RSC Adv.* **2020**, *10*, 33544–33548. [[CrossRef](#)] [[PubMed](#)]
75. Wang, P.; Luo, S.; Boyle, L.; Zeng, H.; Huang, S. Controlled fractal growth of transition metal dichalcogenides. *Nanoscale* **2019**, *11*, 17065–17072. [[CrossRef](#)] [[PubMed](#)]
76. Samaniego-Benitez, J.E.; Mendoza-Cruz, R.; Bazán-Díaz, L.; Garcia-Garcia, A.; Arellano-Jimenez, M.J.; Perez-Robles, J.F.; Plascencia-Villa, G.; Velázquez-Salazar, J.J.; Ortega, E.; Favela-Camacho, S.E.; et al. Synthesis and structural characterization of MoS<sub>2</sub> micropylamids. *J. Mater. Sci.* **2020**, *55*, 12203–12213. [[CrossRef](#)]
77. Ly, T.H.; Zhao, J.; Kim, H.; Han, G.H.; Nam, H.; Lee, Y.H. Vertically Conductive MoS<sub>2</sub> Spiral Pyramid. *Adv. Mater.* **2016**, *28*, 7723–7728. [[CrossRef](#)] [[PubMed](#)]
78. Zhou, Q.; Su, S.; Cheng, P.; Hu, X.; Gao, X.; Zhang, Z.; Liu, J.M. Vertically conductive MoS<sub>2</sub> pyramids with a high density of active edge sites for efficient hydrogen evolution. *J. Mater. Chem. C* **2020**, *8*, 3017–3022. [[CrossRef](#)]
79. Negri, M.; Francaviglia, L.; Kaplan, D.; Swaminathan, V.; Salviati, G.; Fontcuberta, I.; Morral, A.; Fabbri, F. Excitonic absorption and defect-related emission in three-dimensional MoS<sub>2</sub> pyramids. *Nanoscale* **2022**, *14*, 1179–1186. [[CrossRef](#)] [[PubMed](#)]
80. Komen, I.; van Heijst, S.E.; Conesa-Boj, S.; Kuipers, L. Morphology-induced spectral modification of self-assembled WS<sub>2</sub> pyramids. *Nanoscale Adv.* **2021**, *3*, 6427–6437. [[CrossRef](#)]
81. Sarma, P.V.; Kayal, A.; Sharma, C.H.; Thalukulam, M.; Mitra, J.; Shaijumon, M.M. Electrocatalysis on Edge-Rich Spiral WS<sub>2</sub> for Hydrogen Evolution. *ACS Nano* **2019**, *13*, 10448–10455. [[CrossRef](#)]
82. Lin, X.; Liu, Y.; Wang, K.; Wei, C.; Zhang, W.; Yan, Y.; Li, Y.J.; Yao, J.; Zhao, Y.S. Two-Dimensional Pyramid-like WS<sub>2</sub> Layered Structures for Highly Efficient Edge Second-Harmonic Generation. *ACS Nano* **2018**, *12*, 689–696. [[CrossRef](#)]
83. Chen, L.; Liu, B.; Abbas, A.N.; Ma, Y.; Fang, X.; Liu, Y.; Zhou, C. Screw-Dislocation-Driven growth of Two-Dimensional few-layer and pyramid-like WSe<sub>2</sub> by sulfur-assisted Chemical Vapor Deposition. *ACS Nano* **2014**, *8*, 11543–11551. [[CrossRef](#)]
84. Lin, X.; Liu, Y.; Wang, K.; Liu, X.; Yan, Y.; Li, Y.J.; Yao, J.; Zhao, Y.S. Hybrid three-dimensional spiral WSe<sub>2</sub> plasmonic structures for highly efficient second-order nonlinear parametric processes. *Research* **2018**, *2018*, 4164029. [[CrossRef](#)]
85. Shi, W.; Lin, M.L.; Tan, Q.H.; Qiao, X.F.; Zhang, J.; Tan, P.H. Raman and photoluminescence spectra of two-dimensional nanocrystallites of monolayer WS<sub>2</sub> and WSe<sub>2</sub>. *2D Mater.* **2016**, *3*, 025016. [[CrossRef](#)]
86. Tonndorf, P.; Schmidt, R.; Böttger, P.; Zhang, X.; Börner, J.; Liebig, A.; Albrecht, M.; Kloc, C.; Gordan, O.; Zahn, D.R.T.; et al. Photoluminescence emission and Raman response of monolayer MoS<sub>2</sub>, MoSe<sub>2</sub>, and WSe<sub>2</sub>. *Opt. Express* **2013**, *21*, 4908–4916. [[CrossRef](#)] [[PubMed](#)]
87. Tangi, M.; Mishra, P.; Tseng, C.C.; Ng, T.K.; Hedhili, M.N.; Anjum, D.H.; Alias, M.S.; Wei, N.; Li, L.J.; Ooi, B.S. Band Alignment at GaN/Single-Layer WSe<sub>2</sub> Interface. *ACS Appl. Mater. Interfaces* **2017**, *9*, 9110–9117. [[CrossRef](#)] [[PubMed](#)]

88. Zhao, W.; Ghorannevis, Z.; Amara, K.K.; Pang, J.R.; Toh, M.; Zhang, X.; Kloc, C.; Tan, P.H.; Eda, G. Lattice dynamics in mono- and few-layer sheets of WS<sub>2</sub> and WSe<sub>2</sub>. *Nanoscale* **2013**, *5*, 9677–9683. [[CrossRef](#)]
89. Chen, S.; Chen, J.; Zhang, X.; Li, Z.Y.; Li, J. Kirigami/origami: Unfolding the new regime of advanced 3D microfabrication/nanofabrication with “folding”. *Light Sci. Appl.* **2020**, *9*, 75. [[CrossRef](#)]
90. Shinde, S.M.; Dhakal, K.P.; Chen, X.; Yun, W.S.; Lee, J.; Kim, H.; Ahn, J.H. Stacking-controllable interlayer coupling and symmetric configuration of multilayered MoS<sub>2</sub>. *NPG Asia Mater.* **2018**, *10*, e468. [[CrossRef](#)]
91. Cai, L.; Shearer, M.J.; Zhao, Y.; Hu, Z.; Wang, F.; Zhang, Y.; Eliceiri, K.W.; Hamers, R.J.; Yan, W.; Wei, S.; et al. Chemically Derived Kirigami of WSe<sub>2</sub>. *J. Am. Chem. Soc.* **2018**, *140*, 10980–10987. [[CrossRef](#)] [[PubMed](#)]
92. Kastl, C.; Chen, C.T.; Kuykendall, T.; Shevitski, B.; Darlington, T.P.; Borys, N.J.; Krayev, A.; Schuck, P.J.; Aloni, S.; Schwartzberg, A.M. The important role of water in growth of monolayer transition metal dichalcogenides. *2D Mater.* **2017**, *4*, 021024. [[CrossRef](#)]
93. Terrones, H.; Del Corro, E.; Feng, S.; Poumirol, J.M.; Rhodes, D.; Smirnov, D.; Pradhan, N.R.; Lin, Z.; Nguyen, M.A.T.; Elías, A.L.; et al. New First Order Raman-active Modes in Few Layered Transition Metal Dichalcogenides. *Sci. Rep.* **2014**, *4*, 4215. [[CrossRef](#)] [[PubMed](#)]
94. Degregorio, Z.P.; Myers, J.C.; Campbell, S.A. Rational control of WSe<sub>2</sub> layer number via hydrogen-controlled chemical vapor deposition. *Nanotechnology* **2020**, *31*, 315604. [[CrossRef](#)]
95. An, G.H.; Yun, S.J.; Lee, Y.H.; Lee, H.S. Growth Mechanism of Alternating Defect Domains in Hexagonal WS<sub>2</sub> via Inhomogeneous W-Precursor Accumulation. *Small* **2020**, *16*, 2003326. [[CrossRef](#)]
96. Iqbal, M.W.; Shahzad, K.; Akbar, R.; Hussain, G. A review on Raman finger prints of doping and strain effect in TMDCs. *Microelectron. Eng.* **2020**, *219*, 111152. [[CrossRef](#)]
97. Guan, H.; Tang, N.; Huang, H.; Zhang, X.; Su, M.; Liu, X.; Liao, L.; Ge, W.; Shen, B. Inversion Symmetry Breaking Induced Valley Hall Effect in Multilayer WSe<sub>2</sub>. *ACS Nano* **2019**, *13*, 9325–9331. [[CrossRef](#)] [[PubMed](#)]
98. Shen, H.; Ren, J.; Li, J.; Chen, Y.; Lan, S.; Wang, J.; Wang, H.; Li, D. Multistate Memory Enabled by Interface Engineering Based on Multilayer Tungsten Diselenide. *ACS Appl. Mater. Interfaces* **2020**, *12*, 58428–58434. [[CrossRef](#)] [[PubMed](#)]

**Disclaimer/Publisher’s Note:** The statements, opinions and data contained in all publications are solely those of the individual author(s) and contributor(s) and not of MDPI and/or the editor(s). MDPI and/or the editor(s) disclaim responsibility for any injury to people or property resulting from any ideas, methods, instructions or products referred to in the content.